Received 11 February 2021; | Revised 11 February 2021; | Accepted 11 February 2021

DOI: xxx/xxxx

ARTICLE

Fluidized bed hydrodynamic modeling of CO_2 in syngas: Distorted RTD curves due to adsorption on FCC

Ariane Bérard | Bruno Blais | Gregory S. Patience*

[1]Department of Chemical Engineering, Polytechnique Montréal, C.P. 6079, Succ. CV Montréal, H3C 3A7, Québec, Canada

Correspondence
*Corresponding author Gregory Patience, Email: gregory-s.patience@polymtl.ca

Abstract

Bubbles rising through fluidized beds at velocities several times superficial velocities contribute to solids backmixing. In micro-fluidized beds, the walls constrain bubble sizes and velocities. To evaluate gas-phase hydrodynamics and identify diffusional contributions to longitudinal dispersion, we injected a mixture of H_2, CH_4, CO, and CO_2 (syngas) as a bolus into a fluidized bed of porous fluid catalytic cracking catalyst while a mass-spectrometer monitored the effluent gas concentrations at 2 Hz. The CH_4, C_0, and CO_2 trailing RTD traces were elongated versus H_2 demonstrating a chromatographic effect. An axial dispersion model accounted for 92 % of the variance but including diffusional resistance between the bulk gas and catalyst pores and adsorption explained 98.6 % of the variability. At 300 °C, the CO_2 tailing disappeared consistent with expectations in chromatography (no adsorption). H_2 and He are poor gas-phase tracers at ambient temperature. We recommend measuring RTD at operating conditions.

KEYWORDS:
RTD, fluidized bed, microreactor, diffusion, adsorption

1 | INTRODUCTION

The residence time distribution (RTD) is a measure of the general flow patterns of fluids and solids through tanks, pipes, reactors, and processes.[1,2,3,4,5] The method consists of introducing a tagged constituent(s) that tracks the flow path of the gas,[6] liquid,[7] or solid[8] and monitor its concentration with time at the exit or along the vessel length. RTD tests are most applied to experiments but it is increasingly being adapted as a post-processing tool for computational fluid dynamics (CFD) models.[9,10,11] The method assesses back-mixing, dead volumes, channelling, and dispersion by comparing the measured concentration profile against ideal plug flow.

The RTD of the gas phase in fluidized bed reactors is particularly challenging as the hydrodynamics in these systems comprise multiple phases—bubble phase, emulsion phase, jetting at the grid, the splash zone at the top of the bed, and the transport disengagement section.[12] Gas phase diffusion and and adsorption to surfaces contribute to dispersive phenomena that an RTD analysis is capable of identifying.[1] Simple tank-in-series and dispersion models account for much of the variance in the data but more detailed models and measurements with multiple tracers at various temperatures must be applied to better characterize all of the phenomena.[13,14].

Single-phase models disregard heterogeneities like voids (bubbles) and lump all the phenomena into one parameter: The axial dispersion model is an example and the nondimensional Peclet number, $N_{\mathrm{Pe}} = uZ/\mathcal{D}$, is the fitted parameter to characterize the flow where $\mathcal{D}$ is the axial dispersion coefficient. The nondimensional form is:[15,10,16]

$$\frac{\partial C}{\partial \theta} + \frac{\partial C}{\partial \xi} = \frac{1}{N_{\mathrm{Pe}}} \frac{\partial^2 C}{\partial \xi^2} \tag{1}$$

where C is the concentration, θ is nondimensional time ($\theta = tu/Z$) and ξ is the nondimensional length ($\xi = z/Z$).

Researchers apply two phase models to fluidized beds to account for mass transfer between bubbles that form at the grid and the dense emulsion phase. Even these models are crude approximations as they ignore bubble growth, coalescence, splitting, and jets. More detailed models consider the cloud region at the edge of the bubbles and the wake region below.[17,18] Mass transfer between the bubble and the emulsion phase becomes:[19]

$$\frac{dN_A}{dt} = u_b V_{bubble}\left(\frac{dC_{A,b}}{dz}\right) = K_{GB} V_{bubble}(C_A^i - C_{A,b}) \quad (2)$$

where N_A is the mol of A, u_b is the bubble rise velocity, V_{bubble} is the volume occupied by the bubble phase, K_{GB} is the interchange coefficient between bubble and emulsion-cloud, C_A^i is the concentration of A at gas-particle interface, and $C_{A,b}$ is the concentration of A in the bubble.

The second approach merges the cloud and the bubble into a single phase and the second phase is the emulsion. The mass transfer balance is:[20]

$$\frac{dN_A}{dt} = V_{cloud}\left(\frac{dC_{A,c}}{dt}\right) \quad (3)$$

$$= K_{GC} V_{cloud}(C_{A,e} - C_{A,c}) \quad (4)$$

$$= k_{GC} S_{ex,cloud}(C_{A,e} - C_{A,c}) \quad (5)$$

where, the index c represents cloud and e represents emulsion, V_{cloud} is the volume occupied by cloud and bubble, K_{GC} is the interchange coefficient between bubble-cloud and emulsion, k_{GC} is the mass transfer coefficient between bubble-cloud and emulsion, and $S_{ex,cloud}$ is the exterior surface of clouds.

Finally, to approximate reality more closely, the 3-phase model introduces powder physico-chemical properties—porosity, and mass transfer from the gas in the emulsion to the particle surface. First, the flux equation for each phase is[21]:

$$w_p = U_{g,p} C_p - M_{m,p}\frac{\partial C_p}{\partial x} \quad (6)$$

where w is the mass flux, C is the mass concentration, U_g is the gas velocity, and M is the axial mixing coefficient. The index p represents the phases: emulsion (E), bubble (B), or solid (S). Additionally, the continuity equation for each phase is[21]:

$$\frac{\partial w_p}{\partial x} + \frac{\partial C_p}{\partial t} = r_p \quad (7)$$

where r is the reaction rate. To solve equations 6 and 7 for three phases (E, B, and S), we suppose that the velocity and mixing coefficient of the solid phase is negligible ($u_S = M_S \approx 0$)[21].

The models proposed in the literature for RTD analysis in fluidized bed reactors have limitations:

1. Lack of the gas mass transfer mechanism between the pores inside the catalyst and its surface.
2. In general, reaction concepts are missing. Consequently, when adsorption occurs between the tracer and catalyst. The results diverge from the axial dispersion model.
3. Normally only single tracers are modeled. They may or may not characterize the system correctly (Ar and Kr radioactive gas tracers are excellent tracers but are poor models for hydrogen or methane). Each gas tracer is modeled independently. The injection of several tracers demonstrates how the hydrodynamics depend on the gas diffusivity (but this is most evident at ambient temperature).

Here, we analyze the contribution of powder porosity to the residence time distribution of a micro-fluidized bed. We inject a syngas mixture across both Geldart group A and B powders with a syngas gas mixture a (CO_2, H_2, CO, and CH_4) and an MS monitors the mass fraction of each continuously at the exit. Diffusional phenomena predominate for all powders and all constituents at 300 °C but CO_2 adsorption increases the residence time by over 50 % at ambient temperature. We propose a multicomponent model that ignores bubble dynamics in favour of diffusion from the bulk phase to the catalyst pore and adsorption.

2 | EXPERIMENTAL

2.1 | Powders

We compared Fluid Catalytic Cracking Catalyst (FCC) from Total© with sand. FCC is a porous Geldart group A powder while sand is non-porous and belongs to the Geldart group B classification.[22] SEM images demonstrate the spherical shape of FCC and the angular shape of the sand (Figure 1). We confirmed the sphericity by applying the Ergun equation ($\phi_{FCC} = 0.99$ and $\phi_{sand} = 0.68$) :

$$\frac{\Delta P}{\Delta Z} = \frac{U_g}{\phi d_p}\frac{1-\epsilon_v}{\epsilon_v^3}\left(150(1-\epsilon_v)\frac{\mu}{\phi d_p} + 1.75\rho_g U_g\right) \quad (8)$$

where ΔP is the pressure drop, ΔZ is the bed height, ϵ_v is the void fraction, and μ is the viscosity.

The Hausner ratio (H_r) is similar for both powders but the minimum fluidized velocity (U_{mf}), the bulk density (ρ_b) and the mean particle diameter (d_{50}) are 6, 1.6 and 1.4 times higher, respectively, for sand compared to FCC (Table 1). Conversely, the surface area (S_A) measured by BET is 166 times higher for FCC vs sand.

2.2 | Gases

To examine dispersion, diffusion and adsorption independently we measured the RTD with a syngas mixture from Air

TABLE 1 FCC and sand properties[23]. The uncertainties represent standard deviation.

Property	FCC	Sand	n	Comments
Composition	mixed[1]	Silica (SiO_2)	-	-
Geldart Group	A	B	-	-
U_{mf}, mm s^{-1}	2.2	13	1	-
ρ_b, kg m^{-3}	874(4)	1330(10)	5	Scott density
	850(19)	1370(30)	5	Poured density
	970(10)	1530(50)	5	Tapped density
	950	1430	1	Hg porosimetry
ρ_p, kg m^{-3}	1610	2280	1	Hg porosimetry
ρ_{sk}, kg m^{-3}	2360(2)	2777(5)	10	Gas
ϵ_v	0.44	0.37	1	-
H_r	1.13(3)	1.12(4)	5	Hausner ratio
θ_{angle}, °	24(1)	44(2)	6	Angle of repose
d_{10}, µm	39.4(4)	58(2)	3	Laser diffraction
d_{50}, µm	64.0(6)	87(2)	3	Laser diffraction
d_{90}, µm	104(1)	120(2)	3	Laser diffraction
ϕ	0.99	0.68	1	Ergun equation
S_A, m^2 g^{-1}	93	0.6	1	BET
	35	0.4	1	BJH[2]
v_{pore}, mL g^{-1}	0.14	0.003	1	BJH[2]
d_{pore}, nm	38	21	1	BJH[2]

[1] FCC catalysts include a variety of zeolite crystallite sizes and particle properties[24]

[2] BJH: desorption branch

Liquide© :contains 15 % CO_2, 15.3 % CO, 19.9 % H_2, 14.7 % CH_4, and the balance Ar. The purge gas was argon. These gases have a wide range of diffusivity at 25 °C and 300 °C (Table 2).

TABLE 2 Diffusivities in argon and atomic mass for gases. All diffusivities are calculated with the correlation of Fuller – Schettler – Gidding.[25] This method is available for non-polar gases at 101.25 kPa.

Gases	$\mathscr{D}$ [cm^2 s^{-1}] $T = 25$°C	$\mathscr{D}$ [cm^2 s^{-1}] $T = 300$°C	molar mass [g mol^{-1}]
CO_2	0.150	0.479	44
CO	0.195	0.622	28
CH_4	0.208	0.664	16
H_2	0.796	2.54	2

2.3 | Micro reactor set-up

The experiments were run at ambient temperature in an 8 mm diameter quartz tube 360 mm long (Figure 2). We poured 8.19 g of FCC or 13.5 g of sand to reach, a tapped bed height of 180 mm for both. For all experiments, two Brooks mass flow controllers (MFC) maintained the velocity at 10 mm s^{-1}, which represents a Reynolds number (N_{Re}) of 6.8. We installed a Hiden quadrupole mass spectrometer (MS) with a pulse ion counting (SCEM) detector at the exit of the reactor to monitor the tracer concentration *on-line*.[26] The MS capillary was 0.90 m long, 0.20 mm internal diameter, and operated at 160 °C. A vacuum pump maintained pressure at 6.2×10^{-8} Pa. A manifold with an 8-way valve and two identical sample loops made up the injection system.[1] Because the same MFC injects the tracer into the reactor and the lines are identical with the same number of ports on the 8-way valve, the pressure drop across the two lines are identical and we expect only an imperceptible change in pressure when we turn the valve.

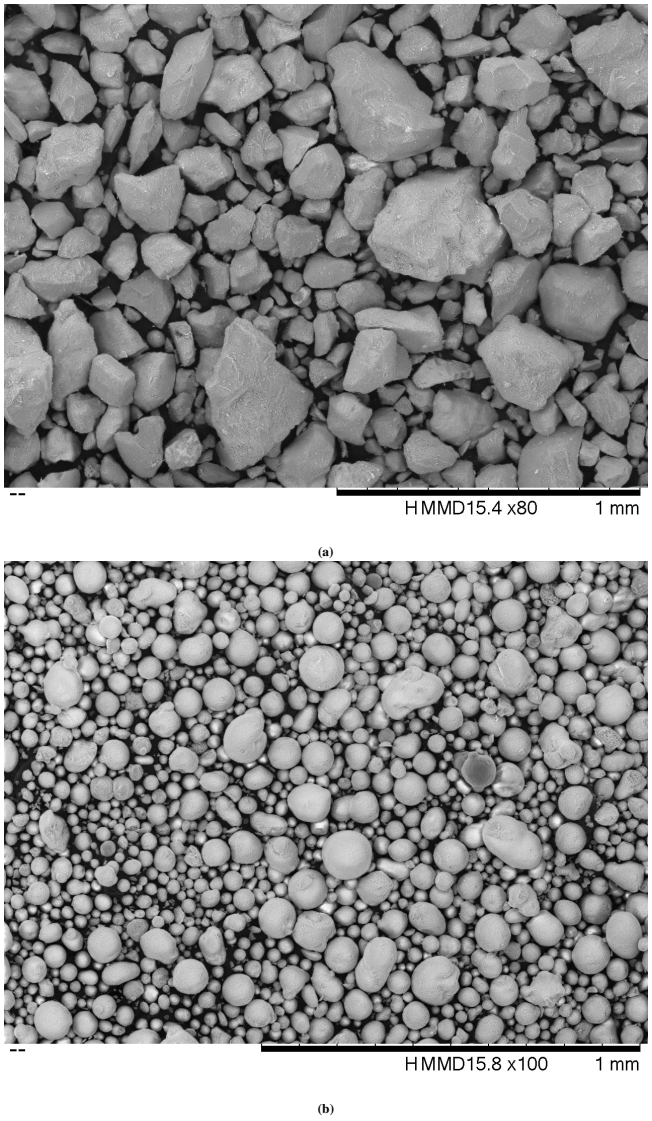

FIGURE 1 SEM images of the powders: (a) Sand—large cuboid or polygonal particles; (b) FCC—most particles are spheroids.

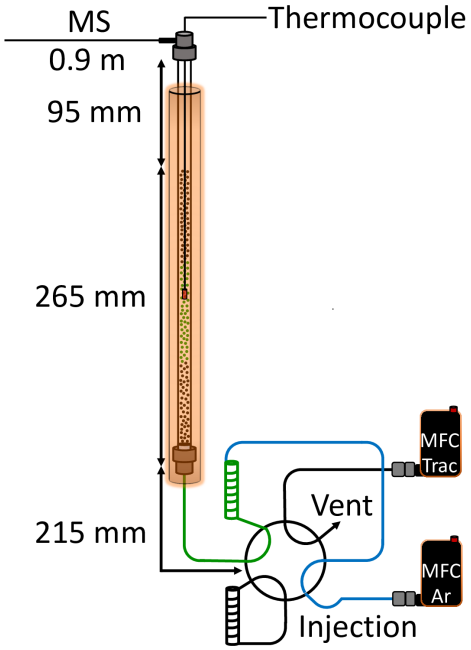

FIGURE 2 Fluidized bed reactor configuration encased in an electrically heated furnace. The quartz tube was 8 mm in diameter and 360 mm long for experiments at 25 °C. For experiments at 300 °C the quartz tube was 320 mm long. At room temperature, the tapped bed height with all catalysts was 180 mm and it expanded to an average of 265 mm when fluidized. At 300 °C, the tapped bed height was 130 mm. The mass spectrometer (MS) capillary was 0.9 mm long with a 0.20 mm internal diameter. First, the 8-way valve is in the filling position (not shown) where argon goes to the reactor and the tracer fills a 10 mL sample loop. Then, at time $t = 180$ s, the 8-way valve switches to the injection position. Argon (blue line) sweeps the tracer (green line) from the loop to the reactor.

The sequence starts with the injection continuously of the inert— argon. Before reaching the reactor, argon passes through the first 10 mL loop. At the same time, the second 10 mL loop fills with tracer (and evacuates to exhaust). After a three minute purge, 8-way valve switched to the injection position and this corresponds to $t = 0$. The argon stream purges the second sample loop with the syngas tracer and enters the reactor. The stream entering the reactor is always controlled with the same MFC. The MS monitored the concentration of all gases simultaneously at 2 Hz for 4 minutes after which we shut off the MS and purge the system with argon for 3 minutes before the beginning another experiment.

For experiments at 300 °C, the reactor is shorter— 32 cm and housed in an electrically heated furnace. The tapped bed height is 13 cm (6.50 g of FCC). We only tested FCC to study the effect adsorption at high temperature. All plastic pipes around the reactor were changed for metal while we kept the same lengths and dimensions. We also added a thermocouple to measure the temperature in the catalytic bed. The experimental sequence was the same.

We minimized dead volume above and below the catalytic bed to minimize the contribution from extraneous lines .[1] For each set of experiments, we performed two RTD tests at the inlet of the reactor, and two at the outlet. For the axial dispersion model, we subtracted the RTD time at the inlet from the RTD trace. For the multi-component model, MS trace below the reactor we considered as the inlet concentration.

2.4 | Axial dispersion model

We fit experimental data with the the axial dispersion model (Equation 1) and applied closed-open boundary conditions:[27,16]

$$C_{0,\xi} = 0, 0 \geq \xi \geq 1 \tag{9}$$

$$C_{\tau,0} = \rho_0, \tau > 0 \tag{10}$$

$$\frac{dC_{\tau,1}}{d\xi} = 0, \tau > 0 \tag{11}$$

The exact analytic solution is:[16]

$$G(\theta) = \frac{1}{2}\left[\text{erfc}\sqrt{\frac{N_{\text{Pe}}}{4\theta}(1-\theta)} + e^{N_{\text{Pe}}}\text{erfc}\sqrt{\frac{N_{\text{Pe}}}{4\theta}(1+\theta)}\right] \tag{12}$$

For each test, we normalized the data to reach the same area under the curve for each gas.

$$\text{Area} = \frac{C_i}{\sum C_i \Delta t} \tag{13}$$

Then, we subtracted the initial time measured at the inlet of the reactor (MS capillary and inlet lines) to the total time at the exit. We minimized the sum of squares of the error (SSE) between the axial dispersion model and the experimental data to calculate N_{Pe}. Finally, to quantify the difference between the predictions and the data, we calculated the coefficient of determination (R^2).

The model adequately approximates pulse injections (no back-mixing) when we simulate each gas independently but the parameters for each gas are different, which confirms that gas diffusion is constributing factor to dispersion. So, we developed a model for multiple-gas injection to account for the difference and the long tail (due to adsorption).

2.5 | New Model-Mole balance equation

Reactor RTD analysis includes multiple phases and species particularly for porous solids and flow systems like fluidized beds. The literature considers an emulsion phase, a bubble phase and at times a cloud phase and a wake. Since the bubble phase is assumed to have little catalyst, all reaction takes place in the emulsion phase (and cloud and wake). Here, we consider that bubbles form and disintegrate sufficiently rapidly that the gas phase is a continuum. Indeed, researchers achieve 100 % conversion in fluidized bed reactors which implies a rapid mixing between the bubble phase and the other phases. Consequently, this phase is neglected in the new model.[28] We consider catalyst as a distinct phase—solid phase. The third phase is the catalyst surface in its pores on which any species may adsorb. Thus, the new model considers three mole balances—the gas phase moving upwards, gas in the pores that follow the movement of the solids, and the adsorbed species on the catalyst surface (that also follow the solids motion). For the injection of multiple tracers, all gas species are dependent on each other. In fact, when a species adsorbs to the catalyst surface, this will have the consequence of reducing the total flow rate in the reactor. We included this dependence when we solved the model. The flow chart (Figure 3) encompasses the principal steps of solving the model.

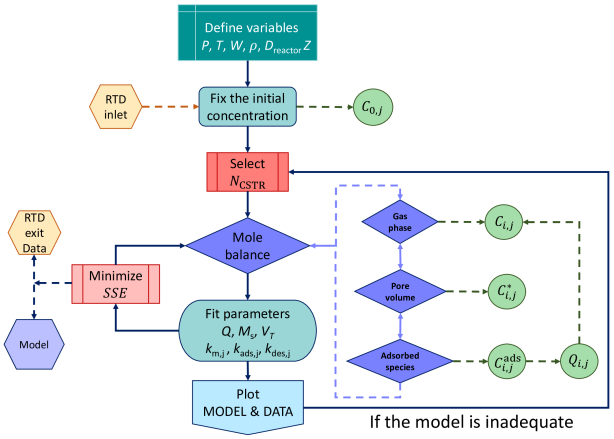

FIGURE 3 Flow chart of the resolution of the multi-component model. Diamonds are equations to solve, hexagons are experimental data, and circles are the species concentrations j in each zone/component. The model is inadequate if the model peak diverges from the experimental data or the R^2 is smaller compared to the axial dispersion model. In this case, we modify the number of CSTRs.

2.5.1 | Gas phase mole balance

In fluidized beds, when the gas velocity exceeds U_{mf} (minimum fluidization velocity), the pressure drop, ΔP is essentially constant and proportional to the bed density, $\rho_p(1-\epsilon_v)$, and the mass of catalyst in the reactor, W:

$$\Delta P = \rho_p(1-\epsilon)gZ = \frac{Wg}{X_A} \tag{14}$$

So the molar density, $C_{i,j}$, varies with height, z, according to:

$$C_{i,j} = \frac{P_{i,j}}{RT} = \frac{P_o - \frac{z_{i,j}}{Z}\Delta P}{RT} \tag{15}$$

and the mole fraction ($y_{i,j}$) for each specie is:

$$y_{i,j} = \frac{C_{i,j}}{\sum_j C_{i,j}} \tag{16}$$

As the bed expands, bubbles grow larger but frictional effects are minimal compared to the solids hold-up. Assuming that the pressure drop is negligible introduces an error of at most 1 % with 10 g of catalyst in a reactor that has a diameter of 8 mm. For deep beds, we include the pressure variation with axial distance.

The volume of the gas phase (V_g) is $\epsilon_v V$ while the volume of the gas in the particle phase (V_p) is $(1-\epsilon_v)\epsilon_{sk} V$. The mass transfer coefficient—$k'_{m,j}$—accounts for molecular diffusion from the gas phase into the catalyst pores and r_j is the adsorption/desorption rate, which is proportional to the number of active sites, V_A. A convective term, Q_{rxn}, accounts for mass transfer between the two phases: when a species from the gas phase is in the pore, $C^*_{i,j}$, and adsorbs to a vacant site, V_V, on the catalyst surface creating an adsorbed species $C^{ads}_{i,j}$. This reaction creates a convective flux, that acts like a vacuum. The flux from the bulk gas phase to the pore phase equals the moles adsorbed. When the desorption rate becomes greater than the adsorption rate, the flux reverses and the convective flux is from the pore to the bulk gas phase. Every reaction, r_j, contributes to the molar flux between the phases at each grid block i, $\tilde{Q}_{rxn,i}$:

$$r^k_{i,j} = \left[k_{ads,j} C^{*,k-1}_{i,j}\left(V_T - C^{ads,k-1}_{i,j}\right) - k_{des,j} C^{ads,k-1}_{i,j}\right] W_i V_{pore,i} \tag{17}$$

$$\tilde{Q}_{rxn,i} = \sum_{j=1}^{N_j} r^k_{i,j} \tag{18}$$

where k_{ads} is the forward reaction—adsorption—and k_{des} is the reverse reaction—desorption.

The volumetric flow rate in the axial direction $Q^k_{i,j}$ is:

$$Q^k_{i,j} = Q^k_{i-1,j} + r^k_{i,j} \tag{19}$$

The axial volumetric flow rate at any height, Q_i, equals the inlet flow rate, Q_o, multiplied by the expansion due to the change in pressure plus the sum of the species that have adsorbed or desorbed to that point.

$$Q_i = Q_o \frac{P_o}{P_i} + Q^k_{i,j} \tag{20}$$

The differential form of the gas phase mole balance is:

$$\frac{\partial C}{\partial t} + U_g \frac{\partial C}{\partial z} = \mathcal{D}\frac{\partial^2 C}{\partial z^2} + k_m(C - C^*) + \frac{y^{k-1}_{i,j}\tilde{Q}_{rxn,i}}{V_g} \tag{21}$$

With the finite volume approach form, when the adsorption rate is greater than the desorption rate ($k_{ads} C^*_i V_T > k_{des} C^{ads}_i$) the mole balance equation for species j in grid block i in the gas phase is:

$$\epsilon_v V \frac{C^k_{i,j} - C^{k-1}_{i,j}}{\Delta t} = -Q^{k-1}_i \left(C^{k-1}_{i,j} - C^{k-1}_{i-1,j}\right)$$

$$-k'_{m,j}\left(C^{k-1}_{i,j} - C^{*,k-1}_{i,j}\right) - y^k_{i,j}\tilde{Q}_{rxn,i} \tag{22}$$

where, $k'_{m,j}$ is a fitting parameter. As gas species j adsorbs onto the catalyst surface the accompanying influx of gas from the bulk gas to the pore is the product of the total moles reacted at that grid block multiplied by the mole faction of that species, $\tilde{Q}_{rxn,i}$.

When the adsorption rate is less than the desorption rate, the net flux is from the pore with a mole fraction y^* multiplied by the total moles of gas that evolve from the surface during that time step: ($k_{ads} C^*_i V_T < k_{des} C^{ads}_i$)

$$\epsilon_v V \frac{C^k_{i,j} - C^{k-1}_{i-1,j}}{\Delta t} = -Q^{k-1}_i \left(C^{k-1}_{i,j} - C^{k-1}_{i-1,j}\right)$$

$$-k'_{m,j}\left(C^{k-1}_{i,j} - C^{*,k-1}_{i,j}\right) + y^{*,k-1}_{i,j}\tilde{Q}_{rxn,i} \tag{23}$$

2.5.2 | Pore volume mole balance

The hydrodynamics of the gas in the pore as well as the adsorbed species is dictated by the transport of the solids phase. The solids move up predominantly in the centre of the vessel and down along the the walls. This motion is well characterized for spouted beds, riser reactors, and larger sized fluidized beds. This movement ensures isothermal conditions and that the solids are perfectly backmixed. To represent it mathematically, we introduce a solids circulation term, M_s, (convective) in both the upward and downward directions and assume radial uniformity—perfectly backmixed). The mass flux, w_s, equals the quotient of the solids circulation rate and the cross-sectional area. The gas velocity (U_g) is:

$$U_g = \frac{w_s}{\rho_p} = \frac{M_s}{X_A \rho_p} \tag{24}$$

where ρ_p is the particle density. The bulk density and skeletal densities are:

$$\rho_b = \rho_p(1 - \epsilon_v) \tag{25}$$

$$\rho_{sk} = \frac{\rho_p}{1 - \epsilon_{sk}} \tag{26}$$

The convective contribution to the mole balance of the pore phase ($\tilde{Q}_{rxn,i}$) is analogous to that of the the gas phase mole balance. The differential form of the pore volume mole balance is:

$$\frac{\partial C^*}{\partial t} = \mathcal{D}_S \frac{\partial^2 C^*}{\partial z^2} - k_m(C - C^*) + W_i\left[k_{ads} C^*(C_T - C^{ads}) - k_{des} C^{ads}\right] \tag{27}$$

where $\mathcal{D}_S$ is the dispersion coefficient for the solid phase.

When the adsorption rate is greater than the desorption rate ($k_{ads} C^*_{i,j} V_T > k_{des} C^{ads}_{i,j}$):

$$(1-\epsilon_v)\epsilon_{sk}V\frac{C_{i,j}^{k,*}-C_{i-1,j}^{k-1,*}}{\Delta t}=\frac{M_s}{\rho_p}\left(C_{i+1,j}^{*,k-1}-C_{i,j}^{*,k-1}\right)-\frac{M_s}{\rho_p}\left(C_{i,j}^{*,k-}\right.$$
$$+k'_{m,j}\left(C_{i,j}^{k-1}-C_{i,j}^{*,k-1}\right)+y_{i,j}^{k-1}\tilde{Q}_{rxn,i}+r_{i,j}^{k-1} \quad (28)$$

and when the desorption rate is greater:

$$(1-\epsilon_v)\epsilon_{sk}V\frac{C_{i,j}^{k,*}-C_{i-1,j}^{k-1,*}}{\Delta t}=\frac{M_s}{\rho_p}\left(C_{i+1,j}^{*,k-1}-C_{i,j}^{*,k-1}\right)-\frac{M_s}{\rho_p}\left(C_{i,j}^{*,k-}\right.$$
$$+k'_{m,j}\left(C_{i,j}^{k-1}-C_{i,j}^{*,k-1}\right)-y_{i,j}^{*,k-1}\tilde{Q}_{rxn,i}+r_{i,j}^{k-1} \quad (29)$$

2.5.3 | Adsorbed species mole balance

The adsorbed species mole balance resembles the pore volume balance and includes the convective term related to solids motion (M_s) but excludes the gas convection terms (Q_{rxn}). The differential form of the adsorbed species mole balance is:

$$\frac{\partial C^{ads}}{\partial t}=\mathcal{D}_S\frac{\partial^2 C^{ads}}{\partial z^2}+V_{pore}\left[k_{ads}C^*(C_T-C^{ads})-k_{des}C^{ads}\right] \quad (30)$$

And, with the finite volume approach is:

$$W_i\frac{C_{i,j}^{ads,k}-C_{i-1,j}^{ads,k-1}}{\Delta t}=-M_s\left(2C_{i,j}^{ads,k-1}-C_{i,j}^{ads,k-1}-C_{i+1,j}^{ads,k-1}\right)- \quad (31)$$

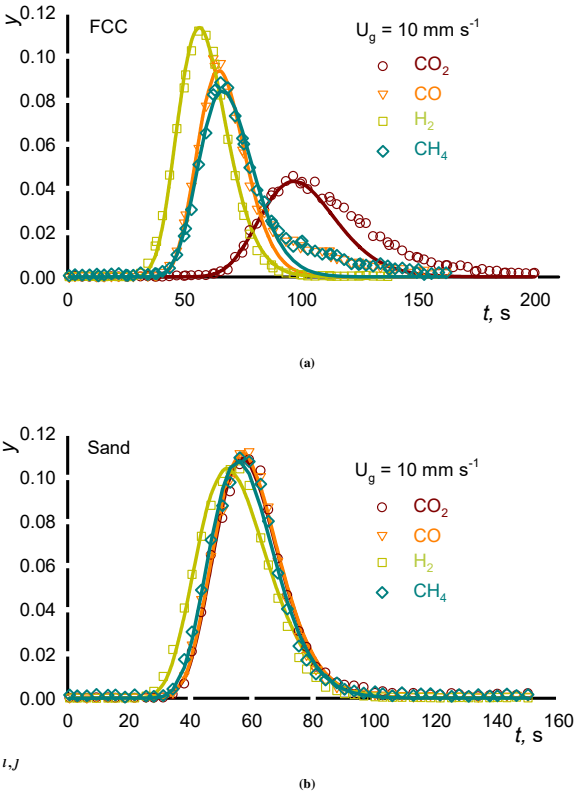

FIGURE 4 RTD comparison between Geldart group A and B catalyst: time vs mole fraction, y. The tube was loaded with (a) 8.19 g of FCC — Geldart group A - and (b) 13.5 g of sand — Geldart group B. For FCC (a), the model fits up to the leading edge of the plot, but not the tail where a deviation is observed for CO_2, CO and CH_4. For sand (b), the axial dispersion model fits perfectly the data for all tracers.

3 | RESULTS AND DISCUSSION

3.1 | Porosity and Geldart group A, B powders

We analyzed the RTD with a pulse input of a mix of tracers including CO_2, CO, H_2, and CH_4 with FCC (Figure 4–a). Diffusivity coefficients for each gas at 25 °C are 0.150 , 0.195 , 0.796 and 0.208 cm^2 s^{-1}, respectively. Based on previous studies, at high velocity in an empty tube the RTD curve is asymmetric with an extended tail. To minimize the tailing, we operated the reactor at $U_g = 10$ mm s^{-1}. The surface area of the FCC is 93 m^2 g^{-1}. The RTD curves for all gases, except for H_2, were superimposed for tests with an empty tube. The residence time varied with diffusivity with FCC loaded to the reactor (Figure 4–a): At $t = 28$ s, the MS first detects hydrogen, and the axial dispersion model characterizes the data very well ($R^2 = 0.990$); 15 s later the MS begins to detect CO and CH_4 (both have similar diffusivity coefficients). When the trailing edge drops to 80 % of the peak height, the curve deviates from an ideal plug flow and the concentration drops more slowly, which corresponds to a long tail. Finally, another 12 s later, CO_2 appears—the peak height is much smaller and the tail much longer.

The time it takes for the tracer to reach the MS after the valve switch is the same for both the step-input and pulse. But the axial dispersion model fits the step-input pulse data very well compared to the pulse, which demonstrates that its applicability to identify anomalies and flow heterogeneity is poor (Figure 5).

We repeated a series of tests with sand with hardly any porosity and a surface area of only –2 m^2 g^{-1} (Figure 4–b). The RTD curves for CO, CO_2 and CH_4 resemble that of the empty tube—all three curves are superimposed and the axial dispersion model fits the experimental data very well. Hydrogen egressed the reactor first due to his high diffusivity coefficient, which is again consistent with the previous study about empty tube experiments. We attribute the difference between FCC and sand RTD to

1. **Diffusion**: hydrogen has a diffusivity coefficient four to five times higher than CO, CO_2 and CH_4 (0.796 vs 0.150 to 0.208 cm^2 s^{-1}). Thus, for RTD experiment with FCC and sand, H_2 exit the reactor 10 to 15 s before CO

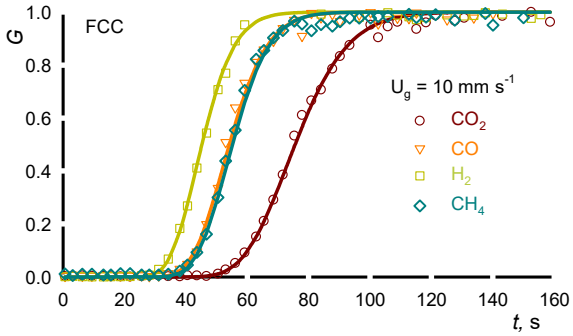

FIGURE 5 RTD for a step injection at 10 mm s^{-1} with 8.19 g FCC. Argon was initially injected. At $t = 0$, the 4-way valve switched to substitute the Ar with feed gas—CO_2, CO, H_2, and CH_4. The dots represent experimental data while the continuous lines are the fitting axial dispersion model. The tail is impossible to detect with a step injection as opposed to the pulse injection.

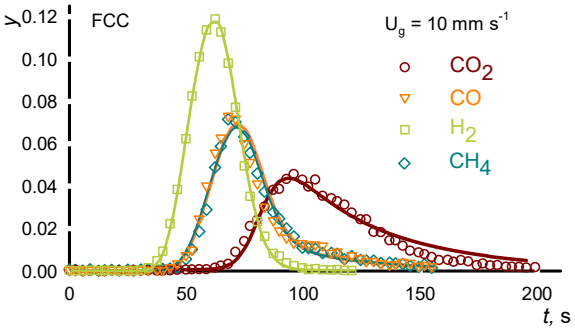

FIGURE 6 New model fitting results for FCC. Same conditions as Figure 4. The model predicts dispersion, diffusion, and adsorption phenomena.

at 10 mm s^{-1}. Radial diffusion of hydrogen ensures a flat concentration profile so that axial dispersion model fits the experimental data well.

2. **Porosity**: The physico-chemical properties of the gas tracer affect the RTD for porous powders more than for non-porous and the effect increases with longer residence time.

3. **Adsorption**: Diffusivity is insufficient to account for the extended CO_2 tail for the case with FCC: The CO_2 RTD curve is delayed by 12 seconds with respect to CO and CH_4. We attribute this delay to a chromatographic effect where CO_2 ingress into the pores and then interacts/adsorbs to the internal surface. With time, the bulk gas concentration decreases and so the driving force reverses and the CO_2 desorbs. This process is on the order of the mixing time of the solids in the bed, which could then extend the residence time (CO_2 adsorbing at the top of the bed is carried down with the solids as the recirculate to the bottom of the reactor).[29]

3.2 | Multi-component model

For each syngas tracer, we applied the new model (Figure 6). We omitted H_2 and resolved simultaneously three mole balances for CO_2, CO, and CH_4. Hydrogen has a high diffusivity coefficient and other phenomena that are unaccounted for with the new model.

First, we calculated the molar concentration at each time step and normalized the data to have identical area under the curve for all tracers. The gas concentration detected at the bottom of the reactor (including the entrance lines and the MS capillary) is applied as the initial concentration in the model simulation. To fit the model, we minimized the sum of squares error (SSE) between the data and the new model for all the tracers together (CO_2, CO and CH_4). The parameters adjusted (Table 3) are the volumetric flow rate (Q), the circulation flow (M_s), the mass transfer between the bulk phase and pores ($k'_{m_{CO_2}}$, $k'_{m_{CO}}$, $k'_{m_{CH_4}}$, $k'_{m_{H2}}$), the adsorption rate ($k_{ads_{CO2}}$, $k_{ads_{CO}}$, $k_{ads_{CH4}}$) and desorption ($k_{des_{CO2}}$, $k_{des_{CO}}$, $k_{des_{CH4}}$). When we reached the highest R^2 for the first three tracers, we fit the hydrogen data by minimizing SSE with the flow rate. We maintained CO_2, CO, and CH_4 parameters. For all tracers, we fitted the first 200 s with an optimal number of CSTRs of 40.

The new model predicts the adsorption of CO_2 compared to the axial dispersion model. Indeed, the coefficient of determination (R^2) is higher for the new model versus the axial dispersion model for all species: CO_2 (0.920 vs 0.986), CO (0.946 vs 0.970), CH_4 (0.979 vs 0.986), and H_2 (0.990 vs 0.999). However, the R^2 for CO and CH_4 with the new model is due to the difference in height and a slight shift to the right (Figure 6) while for the axial dispersion model the low R^2 value is due by the deviation in the elongated tail (Figure 4—a).

The multicomponent model is flexible and accounts for simple plug flow to more complex phenomena including adsorption but it ignores bubble dynamics, clouds, and wakes. H_2, with its small size and high diffusivity coefficient has a residence time 16 % lower than expected from a mass balance: it is as if the volumetric flow rate were 22.5 mL min^{-1} rather than 19.3 mL min^{-1} (Table 3). The RTD curves for CO and CH_4 are very close so we assumed the adsorption/desorption rate constants were the same but allowed the mass transfer coefficients between the gas phase and catalyst to vary. The CO_2 adsorption rate constant is orders of magnitude greater than for CO and

TABLE 3 New model parameters adjusted for a pulse injection RTD in a quartz tube loaded with 8.19 g FCC - velocity of 10 mm s^{-1}. M_s is 9.59×10^{-5} for each gases.

Tracer	Q (mL min^{-1})	k'_m (m^3 s^{-1})	k_{ads} (mol^{-1} s^{-1})	k_{des} (mol^{-1} s^{-1})	V_T (mol g^{-1})	R^2
CO_2		0.48×10^{-6}	32000	120		0.986
CO	19.3	20×10^{-6}	4.9	0.070	3.2×10^{-6}	0.970
CH_4		21×10^{-6}	4.9	0.070		0.986
H_2	22.5	3.2×10^{-6}	0	0	0	0.999

CH4. The concentration of the vacant site (V_T) is 3.2 µmol g^{-1}. The tail is well represented with this model ($R^2 = 0.986$).

3.3 | Temperature analysis

To confirm the impact of diffusivity on RTD, we compared empty tube, FCC and sand with a pulse injection at 300 °C (Figure 7). The syngas tracers—CO_2, CO, CH_4, and H_2—are fed at 10 mm s^{-1}. At this temperature, diffusivity coefficients are 0.479, 0.622, 0.664, and 2.54 cm^2 s^{-1} respectively. The first hypothesis was:

- The larger the difference of diffusivity coefficient is between the gases, the larger will be the delay between each RTD curve.

At 25 °C and 300 °C, the hydrogen diffusivity coefficient is 5 times that of CO_2 and 4 times that of CO and CH_4. According to this hypothesis, the MS should detect H_2 much sooner than the others. However, only hydrogen is slightly advanced compared to CO_2, CO and CH_4, which overlap. Thus, if the ratio (Ex. $H_2/CO = 4$) is kept, the delay between RTD curve will be the same. Curiously, at 300 °C the CO_2 egresses at the same time at the other gases with FCC indicating that adsorption is absent (Figure 7–b). Thus we conclude:

1. The experimental technique is capable of identifying the contribution of diffusivity to the RTD when the diffusion coefficient is at least 2 times greater than any other tracer (the curve of the gas with the highest diffusion coefficient shifts to the left). This observation is valid for porous and non-porous powders (Figure 7–b,c).
2. Even at 300 °C and 14 $\times U_{mf}$, the pulse technique is capable of identifying the effect of diffusion coefficient on the RTD (Supplementary file—Figure S2).
3. Small atomic gases like H_2 and He with high diffusivity coefficient will experimentally fit the axial dispersion model for all velocity and temperatures (Figure 7).

4 | CONCLUSION

The residence time distribution of a single tracer detects gross bypassing, dead volume, and backmixing but is incapable of quantifying diffusional mass transfer resistance or and adsorption/desorption kinetics. Multiple gas species with distinct diffusion coefficients increase the confidence in identifying these phenomena. Hydrogen and helium are poor tracers as they egress faster than other gases due to their much greater diffusion coefficient (at ambient temperature). However, at elevated temperature, even though their diffusion coefficients remain higher, they trace the bulk flow equally well as other gas species like CO_2, CO, and CH_4. The multiple component model described herein ignores bubble dynamics yet is capable of characterizing the tracer data very well, approaching $R^2 = 0.99$. The bubbles in the microfluidized bed rose at velocities several fold higher than U_{mf} but the leading edge of the RTD curves were reasonably sharp confirming that bypassing was negligible.

NOMENCLATURE

C—concentration, [] mol L^{-1}
C_A—[A] in the gas, mol L^{-1}
C_A^i—[A] at the gas-particle interface, mol L^{-1}
$C_{A,b}$—[A] in the bubble phase, mol L^{-1}
C^*— concentration gas phase inside a pore, mol L^{-1}
C^{ads}—concentration adsorbed species, mol L^{-1}
$\mathscr{D}$—diffusivity coefficient, cm^2 s^{-1}
D—axial dispersion coefficient, m^2 s^{-1}
D_S—axial dispersion coefficient for solid phase, m^2 s^{-1}
d_p—particle diameter, m
d_{pore} —pore diameter, m
f_i—prediction data
g—gravity, m s^{-2}
H_r —Hausner ratio, dimensionless
K_{GB}—bubble & emulsion/cloud interchange coefficient, s^{-1}
k_{ads}—adsorption coefficient, mol^{-1} s^{-1}
k_{des}—desorption coefficient, mol^{-1} s^{-1}

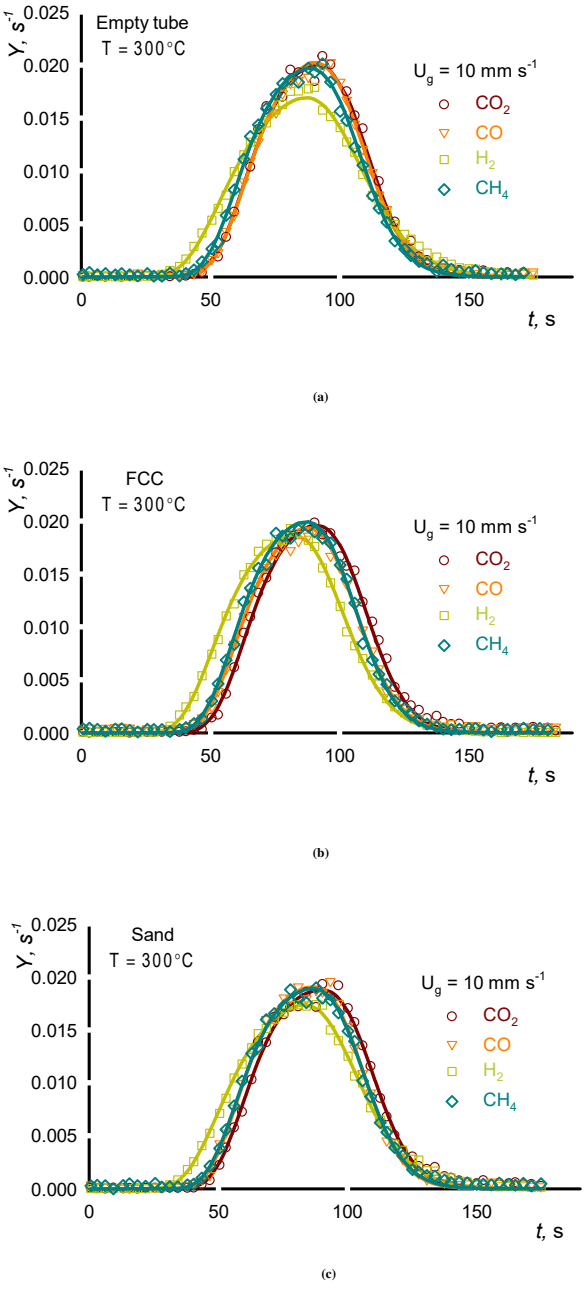

FIGURE 7 Residence time distribution comparison at 300 °C: time vs $Y = \frac{C_i}{\sum C_i \Delta t}$. The quartz tube was (a) empty or loaded with (b) 6.50 g of FCC and (c) 10.7 g of sand. The tapped bed height was 13 cm.

k_{gc}—bubble-cloud/emulsion mass transfer coefficient, m s^{-1}
k'_m—mass transfer coefficient, m^3 s^{-1}
M_m—axial mixing coefficient, m^2 s^{-1}
M_s—solids circulation flow term (convection), kg s^{-1}
N_A—mol of A, mol
N_{Pe}—Peclet number, dimensionless, $[uZ/D]$
N_{Re}—Reynolds number, dimensionless
n_{CSTR}—number of CSTRs in series
P—pressure, Pa
P_o—ambient pressure, Pa
Q_{rxn}—volumetric flow rate / convective term, mL min^{-1}
$\tilde{Q}_{rxn}$—molar flow rate, mol s^{-1}
R—gas constant, [8.314 J mol^{-1} K^{-1}]
R^2—coefficient of determination, dimensionless
r—reaction rate, mol L^{-1} s^{-1}
S_A —specific surface area, m^2 g^{-1}
$S_{ex,cloud}$—exterior surface of clouds m^2
T—temperature, °C
t—time, s
$\bar{t}$—mean residence time, s
U_g—gas velocity, m s^{-1}
U_{mf}—minimum fluidization velocity, m s^{-1}
u_b—bubble rise velocity, m s^{-1}
V—total volume of the system, m^3
V_{bubble}—volume occupied by the bubble phase, m^3
V_{cloud}— volume occupied by cloud and bubble, m^3
V_g — volume of the gas phase, m^3
V_p — volume of the gas in the particle phase, m^3
V_T — number of vacant sites
v_{pore}—specific pore volume, mL g^{-1}
W—mass of catalyst, g
w—flux, kg m^{-2} s^{-1}
w_s—mass flux, kg s^{-1} m^{-2}
X_A—cross sectional area, m^2
y—fraction, dimensionless
$\bar{y}$—mean of experimental data
y_i—experimental data
Z—characteristic system length, m
z—length, m

Greek Letters

ΔP—pressure drop, Pa
ΔZ—bed height, m
ϵ_v—void fraction, dimensionless
ϵ_{sk}—skeletal void fraction, dimensionless
μ — viscosity, kg m^{-1} s^{-1}
ϕ—sphericity, dimensionless
ρ_b—bulk density, kg m^{-3}
ρ_g—gas density, kg m^{-3}
ρ_p—particle density, kg m^{-3}
ρ_{sk}—skeletal density, kg m^{-3}
σ^2—variance, s^2
θ—dimensionless time, $[tu/Z]$
θ_{ang}—angle of repose, °
ξ—dimensionless distance, $[z/Z]$

Indices

c—cloud phase
e—emulsion phase
i—grid
j—species
k —time
p—phase (emulsion (E), bubble (B), and solid (S))

5 | ACKNOWLEDGEMENT

This research was undertaken, in part, thanks to funding from the Canada Research Chairs program and the authors gratefully acknowledge the financial support from the Natural Sciences and Engineering Research Council of Canada (NSERC) and the Canada Foundation for Innovation (CFI).

References

[1] Bérard Ariane, Blais Bruno, Patience Gregory S.. Experimental methods in chemical engineering: Residence time distribution-RTD. *The Canadian Journal of Chemical Engineering.* 2020;98(4):848–867.

[2] Escotet-Espinoza M.S., Moghtadernejad S., Oka S., et al. Effect of tracer material properties on the residence time distribution (RTD) of continuous powder blending operations. Part I of II: Experimental evaluation. *Powder Technology.* 2019;342:744-763.

[3] Stec Magdalena, Synowiec Piotr Maria. Study of Fluid Dynamic Conditions In The Selected Static Mixers Part II-Determination of The Residence Time Distribution. *Canadian Journal of Chemical Engineering.* 2017;95:2410–2422.

[4] Wojewodka P., Aranowski R., Jungnickel C.. Residence time distribution in rapid multiphase reactors. *Journal of Industrial and Engineering Chemistry.* 2019;69:370-378.

[5] Chan C. W., Seville J. P.K., Parker D. J., Baeyens J.. Particle velocities and their residence time distribution in the riser of a CFB. *Powder Technology.* 2010;203(2):187-197.

[6] Andreux R., Petit G., Hemati M., Simonin O.. Hydrodynamic and solid residence time distribution in a circulating fluidized bed: Experimental and 3D computational study. *Chemical Engineering and Processing: Process Intensification.* 2008;47(3):463-473.

[7] Dulle M., Ozcoban H., Leopold C.S.. The effect of different feed frame components on the powder behavior and the residence time distribution with regard to the continuous manufacturing of tablets. *International Journal of Pharmaceutics.* 2019;555:220-227.

[8] Zhang J., Xu G.. Scale-up of bubbling fluidized beds with continuous particle flow based on particle-residence-time distribution. *Particuology.* 2015;19:155-163.

[9] Zou Z., Zhao Y., Zhao H., et al. CFD simulation of solids residence time distribution in a multi-compartment fluidized bed. *Chinese Journal of Chemical Engineering.* 2017;25(12):1706-1713.

[10] Hua L., Wang J., Li J.. CFD simulation of solids residence time distribution in a CFB riser. *Chemical Engineering Science.* 2014;117:264-282.

[11] Li Tingwen, Zhang Yongmin, Grace John R., Bi Xiaotao. Numerical investigation of gas mixing in gas-solid fluidized beds. *AIChE Journal.* 2010;56(9):2280-2296.

[12] Geng Sulong, Han Zhennan, Yue Junrong, et al. Conditioning micro fluidized bed for maximal approach of gas plug flow. *Chemical Engineering Journal.* 2018;351:110–118.

[13] Yang Wen-Ching. Bubbling Fluidized Beds. In: Yang W.-C., ed. *Handbook of fluidization and fluid-particle systems*, New York: Marcel Dekker 2003 (pp. 63–121).

[14] Zhang Jisong, Teixeira Andrew R., Kögl Lars Thilo, Yang Lu, Jensen Klavs F.. Hydrodynamics of gas–liquid flow in micropacked beds: Pressure drop, liquid holdup, and two-phase model. *AIChE Journal.* 2017;63(10):4694-4704.

[15] Hweij K. Abou, Azizi F.. Hydrodynamics and residence time distribution of liquid flow in tubular reactors equipped with screen-type static mixers. *Chemical Engineering Journal.* 2015;279:948-963.

[16] Patience G.S.. Circulating Fluidized Beds: Hydrodynamics and Reactor Modelling. Thesis1990.

[17] Drinkenburg A.A.H., Rietema K.. Gas transfer from bubbles in a fluidized bed to the dense phase—I. Theory. *Chemical Engineering Science.* 1972;27(10):1765 - 1774.

[18] Yang W.C.. *Handbook of Fluidization and Fluid-Particle Systems*. Pittsburgh, Pennsylvania, U.S.A.: Marcel Dekker, Inc.; 2003.

[19] Kunii Daizo, Levenspiel Octave. Fluidization Engineering. In: Kunii Daizo, Levenspiel Octave, eds. *Fluidization Engineering (Second Edition)*, Boston: Butterworth-Heinemann second edition ed.1991 (pp. 1 – 491).

[20] Partridge B.A., P.N. Rowe. Chemical reaction in a bubbling gas fluidised bed. *Trans. Inst. Chem. Engrs.*. 1966;44:335-348.

[21] Wippern D., Wittman K., Kuhne J., Helmrich H., Schügerl K.. Characterizationn of fluidized bed reactors with gas tracer measurements. *Chemical Engineering Communications.* 1981;10(4-5):307-330.

[22] Geldart D.. Types of Gas Fluidization. *Powder Technology.* 1973;7:285–292.

[23] Menéndez Miguel, Herguido Javier, Bérard Ariane, Patience Gregory S.. Experimental methods in chemical engineering: Reactors–fluidized beds. *The Canadian Journal of Chemical Engineering.* 2019;97(9):2383-2394.

[24] Vinnett L., Contreras F., Lazo A., Morales M., Díaz F., Waters K.E.. The use of radioactive tracers to measure mixing regime in semi-autogenous grinding mills. *Minerals Engineering.* 2018;115:41–43.

[25] Vargaftik N.B.. *Handbook of physical properties of liquids and gases*. Springer-Verlag Berlin Heidelberg; 2 ed.1975.

[26] Perreault Patrice, Robert Etienne, Patience Gregory S.. Experimental Methods in Chemical Engineering: Mass Spectrometry—MS. *The Canadian Journal of Chemical Engineering.* 2019;97(5):1036-1042.

[27] Lapidus L., Amundson N. R.. Mathematics of Adsorption in Beds. VI. The Effects of Longitudinal Diffusion in Ion Exchange and Chromatographic Columns. *Journal of Physical Chemistry.* 1952;56:984–987.

[28] Patience G. S., Farrie Y., Devaux J.-F., Dubois J.-L.. Oxidation Kinetics of Carbon Deposited on Cerium-Doped FePO4 during Dehydration of Glycerol to Acrolein. *Chemical Engineering & Technology.* 2012;35(9):1699-1706.

[29] Yates J.G., Constants J.A.P.. Residence time distributions in a fluidised bed in which gas adsorption occurs: stimulus-response experiments. *Chemical Engineering Science.* 1973;28(6):1341 - 1347.